

Development of A Miniaturized 3-DOF Force Sensing Instrument for Robotically Assisted Retinal Microsurgery and Preliminary Results*

Xingchi He¹, *Student Member, IEEE*, Peter Gehlbach², *Member, IEEE*, James Handa²,
Russell Taylor³, *Fellow, IEEE*, Iulian Iordachita¹, *Senior Member, IEEE*

Abstract—Lack of force sensing is one of the most formidable technical challenges in retinal microsurgery. Incorporating high sensitivity force sensing into the ophthalmic tools has the potential to provide the surgeon useful force feedback and to enable safe robotic assistance. This paper presents a new design of a three degrees of freedom force sensing instrument based on fiber Bragg grating sensors. A new flexure is developed to achieve high axial force sensing sensitivity and low crosstalk noise. The force sensing segment of the tool, located directly proximal to the tool tip, is $\varnothing 0.9 \times 8$ mm. An extensive calibration shows that the force sensor can measure the transverse and axial force up to 21 mN with 0.5 mN and 3.3 mN accuracy, respectively. The new flexure design demonstrates the potential to improve axial force sensing. Analysis of the experiment results suggests improvements for the future iteration.

I. INTRODUCTION

Retinal microsurgery involves complex intraocular surgical procedures to treat retina-related diseases, e.g., epiretinal membrane (ERM), diabetic retinopathy, retinal detachment, and macular holes. During retinal microsurgery, the surgeon inserts long, thin ophthalmic instruments through trocars on the sclera to perform fine manipulation of the delicate eye tissue in a small constrained space (average axial length of the human eye is about 23.5 mm), as shown in Fig. 1. One challenge to treatment stems from the microscopic dimensions and the fragility of the tissues in the eye. Another challenge derives from the human physiological limitations, such as surgeon hand tremor and fatigue. One of the most formidable technical challenges is the lack of force sensing. Forces exerted in retinal microsurgery are generally well below the human sensory threshold. Previous study [1] has shown that 75% of forces applied during *in vitro* retinal manipulation in porcine cadaver eyes are less than 7.5 mN, and only 19% of the events at this force level can be felt by the surgeons. Large forces are undesired and can potentially damage the delicate retina. Incorporating force sensing capability into the ophthalmic instrument enables

quantitative monitoring of force applied during retinal microsurgery. It can be used to provide awareness of subtactile tool-tissue forces to the surgeon. The technology can also be incorporated into robotic systems to provide haptic feedback and motion guidance.

There has been considerable work on force sensing for microsurgery, micromanipulation, and minimally invasive surgery (MIS). Menciassi *et al.* [2] developed a piezo-actuated microgripper with a dimension of $17 \times 0.5 \times 0.4$ mm. The microgripper is instrumented with strain gauges for force sensing to provide haptic feedback in microsurgery. Peirs [3] designed a MIS instrument using intensity modulated optic sensors. It provides triaxial force sensing with a resolution of 0.04 N. Seibold *et al.* [4] utilized a flexure Steward platform with strain gauges to integrate 6-axis force sensing into an actuated MIS instrument. Polygerinos *et al.* [5] developed a triaxial catheter-tip force sensor for MRI-guided cardiac ablation procedures. Furthermore, various studies have investigated different force sensing techniques, such as piezoresistive strain gauges [6]–[9] and fiber optical sensors [10], [11]. However, these designs cannot be directly applied to retinal microsurgery due to the specific requirements on the force sensing range (≥ 10 mN), resolution (≤ 1 mN), and dimensions (e.g., ≤ 0.9 mm in diameter). It is also desired that the force sensor is integrated into the distal portion of the tool shaft, typically located inside the eye. Force sensors mounted in the handle of the microsurgical tool [12] cannot distinguish the force exerted at the tool tip and the contact force at the sclerotomy [13].

Our approach is to integrate fiber optic sensors into the tool shaft, close to the tool tip, such that the sensors are located inside the eye when the tool is used to manipulate the eye tissue. We developed a family of two degrees of freedom (DOF) force sensing tools [14]–[16] that can measure the transverse forces with 0.25 mN resolution. Our previous work has further investigated 3-DOF force sensing instruments using a Fabry-Pérot interferometer [17] and fiber Bragg grating (FBG) [18], [19]. In this paper, we report a new design of a sub-millimetric 3-DOF force sensing instrument with integrated FBG sensors. A new flexure is developed to improve the axial force sensing, and reduce crosstalk noise from the transverse force. The tool design, fabrication, calibration, and experimental results are described in the following sections.

*Research supported in part by NIH BRP grant 1 R01 EB 007969, NIH grant R01 EB 000526, in part by Wilmer Eye Institute's Research to Prevent Blindness, and in part by Johns Hopkins University internal funds. Other equipment and systems infrastructure support were developed within the CISST ERC under NSF grant EEC9731748.

¹Xingchi He and Iulian Iordachita are with the Mechanical Engineering Department, Johns Hopkins University, Baltimore, MD 21218, USA xingchi.he@jhu.edu

²Peter Gehlbach and James Handa are with the Department of Ophthalmology, Johns Hopkins School of Medicine, Baltimore, MD 21287, USA. Dr. Handa is the Robert Bond Welch Professor.

³Russell Taylor is with the Computer Science Department, Johns Hopkins University, Baltimore, MD 21218, USA. Dr. Taylor is the John C. Malone Professor.

TABLE I
DESIGN SPECIFICATIONS OF THE 3-DOF FORCE SENSING INSTRUMENT

| | | |
|-------------------------|---|-----------------|
| Dimension | Tool shaft diameter | ≤ 0.9 mm |
| | Tool shaft length | ≈ 30 mm |
| | Sensing segment length | ≤ 15 mm |
| Sensing performance | Force resolution (X/Y) | ≤ 0.25 mN |
| | Force resolution (Z) | ≤ 1 mN |
| | Force range (X/Y/Z) | ≥ 10 mN |
| | Sampling rate | ≥ 100 Hz |
| Additional requirements | Compatible with the tool quick release mechanism of the Steady-Hand Eye Robot | |

II. DESIGN AND FABRICATION

Retinal microsurgery requires the force sensor to provide high resolution force sensing within strict dimension constraints. To achieve the design specifications, we incorporate high sensitivity FBG sensors with a new flexure design. The force sensor prototype is assembled from components fabricated with photochemical etching and laser micro-machining.

A. Design Requirements

Table I summarizes the design specifications for the 3-DOF force sensing instrument. In order to achieve accurate sensing of the tool-tissue forces, it is important to design a compact force sensor that fits into the distal end of the tool shaft. The diameter of the force sensor needs to be less than the tool diameter (≤ 0.9 mm, i.e., 20 Ga). The length of the force sensor should be less than 15 mm to ensure that the force sensor stays inside the eye with sufficient margin for tool motion.

The desired force range is at least 10 mN, because most of the forces exerted during retinal microsurgery are below 7.5 mN in magnitude [1]. Ophthalmic instruments are long and thin, therefore their axial stiffness is significantly higher than the transverse/bending stiffness. The major design challenge is to integrate axial force sensing with high sensitivity. The desired force resolution is 0.25 and 1 mN for transverse and axial forces, respectively. In addition, we want to integrate the tool quick release mechanism [20] into the tool handle, so that the 3-DOF force sensing tool can be incorporated with the Steady-Hand Eye Robot [20], [21] to enable robot force feedback and force control methods [21]–[23].

B. Force Sensor Concept Design

Previous work by our group [19] demonstrates the 3-DOF force sensing capability using FBG sensors with a miniaturized flexure. One drawback of the flexure design presented in [19] is that the flexure deformation increases under both axial and transverse forces. While reducing the structure stiffness under axial force is desired for improving axial force sensing sensitivity, large bending deformation under transverse force can introduce significant crosstalk noise to interfere axial force sensing. In previous design, this problem is intended to be mitigated by the FBG sensor configuration: first, the FBG sensor for axial force sensing is aligned with the tool axis in order to minimize the crosstalk noise from bending; second, the three FBG sensors for transverse force sensing

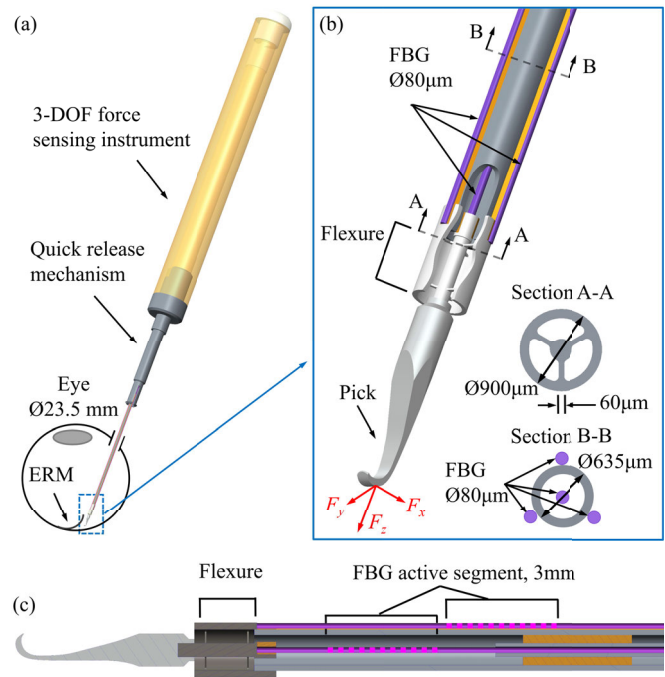


Fig. 1. CAD model of the 3-DOF force sensing instrument. The tool is used to peel off ERM (a). Close-up view of the tool tip force sensing segment (b). Part of the tubular tool shaft is removed to reveal the flexure and FBG sensor in the center of the tool shaft. Section A-A is the section view of the flexure. Section B-B shows the configuration of the FBG sensors. Longitudinal section view of the distal force sensing segment (c). The FBG active segments of the FBG sensors are highlighted with dashed lines in pink.

are placed proximal to the flexure so that they are isolated from the flexure deformation. In this iteration, the flexure design is improved to provide maximum deformation under axial force load and minimum deformation under transverse force load.

Fig. 1 illustrates the sensor design concept. Similar to our 2-DOF force sensing tools [14]–[16], three outer FBG sensors are arranged at 120° intervals along the tubular tool shaft, as shown in Fig. 1(b). They are used to measure the transverse force. Axial force sensing is realized by combining a flexure and an inner FBG sensor. The flexure consists of an outer tube connected to an inner wire by six thin flexible beams. Each beam is $50 \mu\text{m}$ thick, $60 \mu\text{m}$ wide, and $200 \mu\text{m}$ long. The beams are arranged in two separate planes that are 1 mm longitudinally apart. Within each plane, the three beams form a Y-shape configuration with 120° intervals. The distal end of the inner wire is joined with the micro-pick, while its proximal end is connected to the inner FBG sensor that is aligned with the tool axis. Theoretically, this FBG sensor only measures the strain generated by axial force, decoupled from transverse force, because it should be placed on the neutral bending axis, i.e., the tool axis. However, it is difficult to achieve perfect alignment in practice. The flexure should strengthen the decoupling of axial force sensing from the transverse forces, as well as provide axial strain amplification under axial force load. All four FBG sensors have a 3 mm FBG active segment with

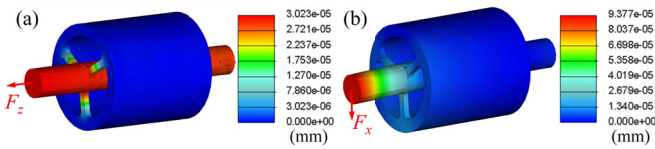


Fig. 2. Displacement of the flexure under 10 mN axial force (a) and that under 10 mN transverse force (b) in FEA simulation. While the displacement is well transferred to the proximal output end under axial force, the displacement is minimized at the output end under transverse force. The material used in the FEA simulation is stainless steel with a Young's modulus of 193 GPa.

center Bragg wavelength of 1545 nm (Technica S.A., Beijing, China). The fiber cladding diameter is 80 μm , while the fiber diameter including the coating is 100 μm .

Finite element analysis (FEA) is carried out using Creo/Simulate (PTC, Needham, MA) to evaluate the flexure behavior under axial and transverse load. Fig. 2 shows the displacement generated in the flexure when 10 mN axial and transverse forces are applied at the distal input end of the inner wire of the flexure, respectively. When axial force is applied, the displacement of the proximal output end (2.8×10^{-5} mm) is close to that of the input end. Under transverse force load with the same magnitude, the displacement of the proximal output end is minimized (3.4×10^{-6} mm). By comparison, FEA simulation with the same force loads are performed with the previous flexure design. The displacement generated by axial and transverse forces are 4.4×10^{-4} mm and 5.8×10^{-3} mm, respectively. Although the new flexure design does not provide the same large strain amplification under axial force as the previous design, it reduces the crosstalk noise from the transverse force by a factor of 1000.

C. Fabrication of the 3-DOF Force Sensing Instrument

The FEA simulation demonstrates that the new flexure design exhibits the desired behaviors, i.e., strain amplification for axial force and noise rejection against transverse force. However, its complex structure and small dimension present challenges for fabrication. An assembly model is devised to fabricate a prototype as a proof of concept. The assembly model consists of components that can be manufactured using photochemical etching and laser micro-machining, as shown in Fig. 3. Two Y-shape beams, (3) and (6), are fabricated with photochemical etching with brass (E-FAB, Santa Clara, CA). The stainless steel tubes, (5) and (10), form the main tool shaft. The inner (ID) and outer diameter (OD) of (5) are 0.7 and 0.9 mm, respectively, while (10) has an ID of 0.43 mm and an OD of 0.635 mm. The stainless steel wire (2) ($\varnothing 0.125$ mm) joins the pick (1), the flexure beams (3) and (6) with the stainless steel tube (4) as spacer between the flexure beams. The stainless steel tube (7) connects the inner wire (2) with distal end of the inner FBG sensor (9). Both (4) and (7) have an ID of 0.15 mm and an OD of 0.31 mm. The proximal side of the inner FBG sensor (9) is fixed by stainless steel tube (8), to align the FBG active segment with the tool axis. The ID and OD of (8) are 0.18

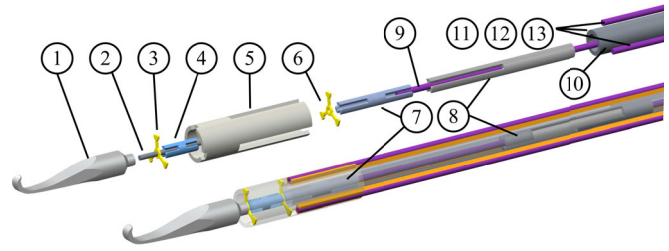


Fig. 3. Assembly model of the 3-DOF force sensing instrument is devised for prototyping. The exploded view (top) and full assembly (bottom) of the distal force sensing segment. In the bottom view, tube (5) and (10) are rendered semi-transparent to show the arrangement of the components inside the tool shaft.

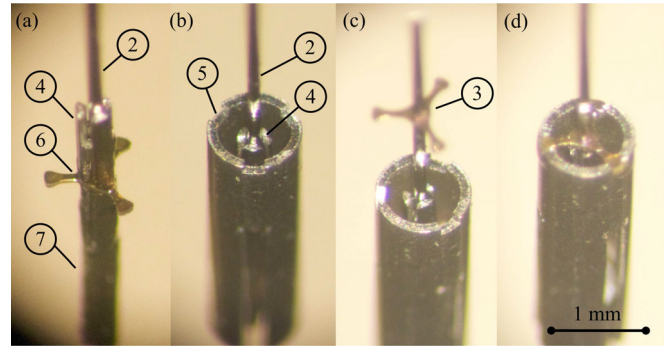


Fig. 4. Major steps in the assembly process of the flexure (a), (b), (c), and the assembled flexure (d). The assembly is oriented with the tool tip pointing upwards.

and 0.36 mm, respectively. The outer FBG sensors (11), (12), and (13) are longitudinally attached to the tool shaft (10), with 120° intervals. All stainless steel tubing is laser micro-machined (Laseraage, Waukegan, IL).

All components are manually assembled under a microscope. Fig. 4 shows the major steps of the flexure assembly process. All connections are adhesive bonding using Loctite 3103 (tensile modulus 207 N/mm², Henkel, CT). First, the center wire (2), spacer (4), flexure beam (6), connector (7), and inner FBG sensor (9) (not shown in Fig. 4(a)) are connected in series. Second, the outer tube (5) is carefully aligned and joined with the flexure beam (6). Third, the second flexure beam (3) is fixed with the outer tube (5) and spacer (4). Fig. 4(d) shows the assembled flexure.

After the flexure is built, the intermediate support tube (8) and the outer tube (10) are added. Subsequently, the outer FBG sensors are attached to the outer tube (10). The final step is to install the tool handle with the quick release mechanism. Fig. 5 illustrates the prototype of the new 3-DOF force sensing instrument. The length of the distal force sensing segment is about 8 mm. Although the micro-pick is not attached in the current prototype, it can be added in the future.

III. EXPERIMENTS AND RESULTS

The new 3-DOF force sensing instrument is calibrated with an automated calibration system [19]. Fig. 6(a) and (b) illustrate the calibration setup. A precision scale is used

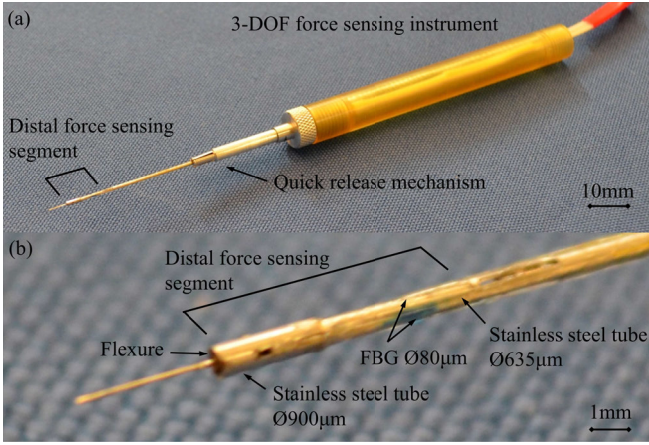


Fig. 5. The prototype of the new 3-DOF force sensing instrument (a). The close-up view of the distal force sensing segment (b).

to measure the force magnitude with 1 mg resolution. A calibration weight (2.15 g) is attached to the tool tip through a thin wire. A high precision robot holds the tool to control its orientation and position. The height of the tool tip with respect to the scale determines the portion of the calibration weight applied on the tool tip, i.e., force magnitude. The two rotational DOFs of the robot, roll and sweep, control the orientation of the tool, thus the direction of the force load. The definition of the roll and sweep angles in the tool tip coordinate is illustrated in Fig. 6(c). The robot translational and rotational resolution are $1 \mu\text{m}$ and 0.005° , respectively. The FBG sensors are sampled with an optical sensing interrogator sm130-700 (Micron Optics, Atlanta, GA) at 2 kHz refresh rate. More details on the calibration system are described in [19].

The 3-DOF force sensing tool is calibrated in 168 poses with the roll α and sweep β angles varying from -165° to 180° , and from 0° to 90° , respectively, both with 15° incremental. Fig. 6(d) illustrates all 168 directions of the calibration force loads. At each pose, the force magnitude ranges from 0 to 21 mN. In total, about 2.4×10^5 calibration samples are obtained. In the following sections, the calibration data is used to determine the mapping from the FBG sensor readings to the transverse and axial forces.

A. Transverse Force Calibration

Our previous work [14], [19] has shown the FBG sensor readings are linearly dependent on the transverse force. The key equation is shown below for readers' convenience with detailed description in [19]:

$$F_t = K_t \Delta S_t \quad (1)$$

where $F_t = [F_x, F_y]^T$ denotes the transverse force applied at the tool tip, K_t denotes a 2×3 coefficient matrix, and $\Delta S_t = [\Delta s_1, \Delta s_2, \Delta s_3]^T$ is the sensor readings of the three outer FBG sensors.

Fig. 7 illustrates the calibration results using linear fitting for transverse force. Fig. 7(a) and (d) show the calculated force versus the actual force, in X- and Y-direction, respectively. A straight line through the origin with slope

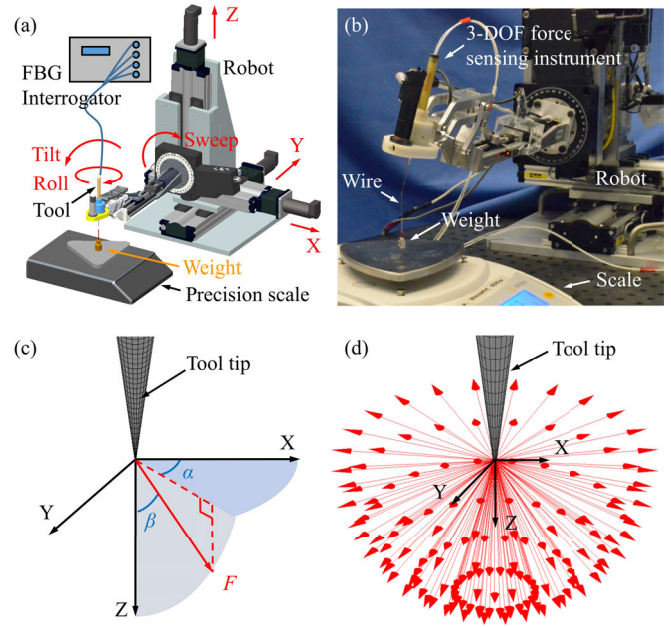


Fig. 6. Setup of the automated calibration system (a). Close-up view of the actual calibration setup (b). Roll angle α and sweep angle β shown in the tool tip coordinate frame (c). All force directions applied in the calibration (d).

1 (45°) would be the perfect fitting result. As shown in Fig. 7(a) and (d), the estimated values of both F_x and F_y are consistent with their actual values. Fig. 7(b) and (e) illustrate the residual errors. The root mean square (RMS) error is 0.53 and 0.36 mN for F_x and F_y , respectively. Fig. 7(e) and (f) show the probability distribution of the residual error. The distribution of residual error in F_x is skewed to the right, while the distribution of residual error in F_y is fairly symmetric. This could indicate that the manual assembly process, together with machining and assembly tolerance, potentially creates structural asymmetry in the 3-DOF force sensing tool.

B. Axial Force Calibration

FEA simulation results in Section II-B show that the new flexure can be less sensitive for axial force sensing, compared to the previous design, despite improved crosstalk noise rejection. We first test a linear model, and then use a polynomial model to calculate the axial force.

A simple linear model for calculating axial force can be written as:

$$F_z = K_z \Delta \Lambda \quad (2)$$

where F_z denotes the axial force, K_z is a 1×4 coefficient vector, and $\Delta \Lambda = [\Delta \lambda_1, \Delta \lambda_2, \Delta \lambda_3, \Delta \lambda_4]^T$ denotes the Bragg wavelength shifts of the FBG sensors. This linear model provides a local estimate for the samples with the sweep angle $\beta \leq 15^\circ$, as shown in Fig. 8(a), (b), and (c). This partial data corresponds to all the forces in a cone region with a vertex angle of 30° . The RMS error is 1.27 mN.

A second-order Bernstein polynomial model is used to

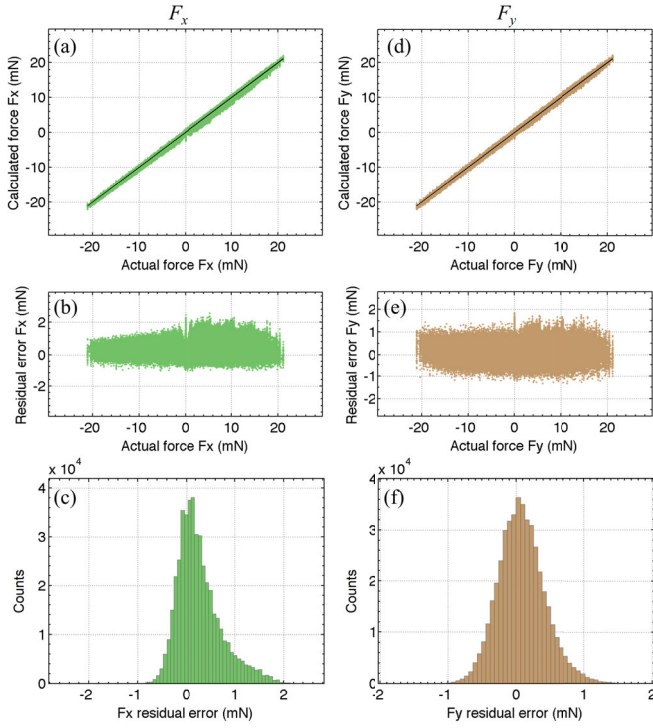


Fig. 7. Results of transverse force calibration. The calculated F_x versus the actual value using linear fitting (a), the residual error (b), and the histogram of the residual error of F_x (c). Accordingly, (d), (e), and (f) are the same plots for F_y .

calculate a global fitting for all calibration data:

$$F_z = \sum_{i=0}^n \sum_{j=0}^n \sum_{l=0}^n \sum_{k=0}^n c_{ijkl} b_{i,n} b_{j,n} b_{k,n} b_{l,n} \quad (3)$$

where $n = 2$ is the order of the Bernstein polynomial, F_z denotes the axial force, c_{ijkl} denotes the coefficients, $b_{i,n} (\Delta\lambda_1^*)$, $b_{j,n} (\Delta\lambda_2^*)$, $b_{k,n} (\Delta\lambda_3^*)$, and $b_{l,n} (\Delta\lambda_4^*)$ are the Bernstein basis polynomials. More detailed description on Bernstein polynomial is in [19].

As shown in Fig. 8(d), (e), and (f), the polynomial fitting exhibits relatively large error. The RMS error is 3.33 mN, and the maximum residual error is greater than 10 mN. The possible reasons for the large fitting error is discussed in Section IV.

IV. DISCUSSION

A. Behavior of the Inner FBG Sensor

The inner FBG sensor is devoted to measuring the axial force, leveraging strain amplification and crosstalk noise rejection provided by the flexure design. However, experimental results in Section III-B indicate that the sensor behavior differs from the design expectation. The Bragg wavelength shift of the inner FBG sensor, $\Delta\lambda_4$, is reviewed carefully with the force load applied. It is found that $\Delta\lambda_4$ is linearly correlated to the force magnitude in each force direction, i.e., given α and β ,

$$\Delta\lambda_4 \approx \kappa \|F\| + c \quad (4)$$

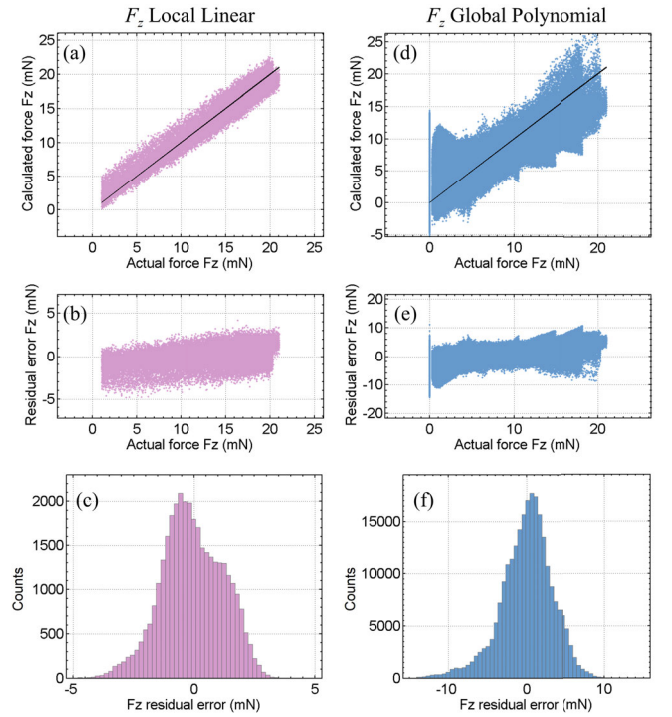


Fig. 8. Results of axial force calibration. The calculated F_z using linear fitting versus the actual value on the samples with sweep angle $\beta \leq 15^\circ$ (a), the residual error (b), and the histogram of the residual error of F_z (c). Accordingly, (d), (e), and (f) are the same plots for all samples using second-order Bernstein polynomial.

where $\|F\|$ is the force magnitude, κ and c denote the slope and the offset of the linear relationship, respectively. The correlation coefficients between $\|F\|$ and $\Delta\lambda_4$ at all 168 poses (combination of 24 roll α and 7 sweep β angles) have a mean of 0.95, with standard deviation of 0.06. The inner FBG sensor exhibits local linearity with respect to the force magnitude. However, the slope κ varies with the force direction, which is determined by α and β . Fig. 9(a) and (b) illustrate κ values calculated in each force direction plotted on the α - β grid and on a unit hemisphere, respectively. For better visualization, linear interpolation is used to generate a finer grid/hemisphere with 5° incremental from the original with 15° incremental. First, large variation in κ occurs when β gets close to 90° , i.e., the force load turns toward the transverse direction. This corresponds to the peak and valley along α -axis when $\beta \rightarrow 90^\circ$, as shown in Fig. 9(a). One possible cause could be that the inner FBG sensor is slightly off the tool axis. Second, although the κ values where α is between 0° and 60° are relatively close, there are still small fluctuations, forming many local humps, as shown in Fig. 9(a). This small variation could be due to the nonuniform structural behavior of the miniature, yet complex prototype assembly.

As comparison, Fig. 9(c) and (d) illustrate the κ values calculated using the calibration data of the previous 3-DOF force sensing tool [19]. First, κ presents an even larger shift along α -axis, when β increases to 90° . When the force direction is near transverse, κ can drop below zero.

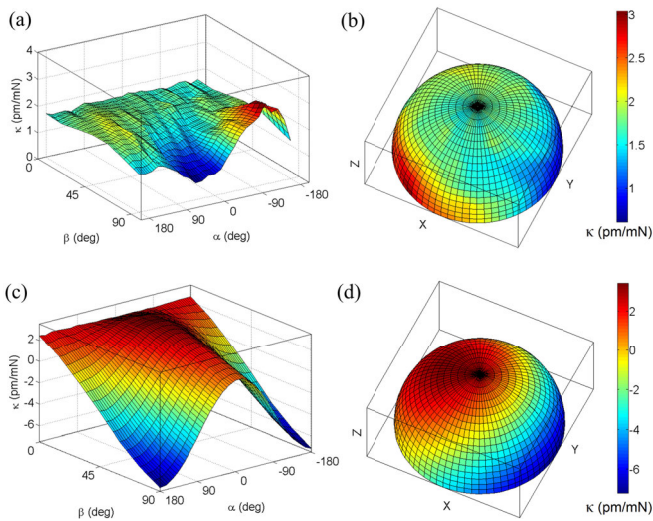


Fig. 9. The ratio κ between the Bragg wavelength shift of the center FBG $\Delta\lambda_4$ and the force magnitude plotted on the α - β grid (a), and that plotted on a unit hemisphere (b). Same plots (c) and (d) are generated with the calibration data from previous design.

This indicates that the bending due to the transverse force component dominates the tension attributed to the axial force component, resulting in a negative slope between the force magnitude and the Bragg wavelength shift. This observation confirms the drawback of the previous flexure design as mentioned in Section II-B. As shown in Fig. 9(a), the new flexure design improves on suppressing the variation of κ with respect to changes of β . Compared to the previous design, it provides a more consistent sensor response as the force direction sweeps between transverse and axial. While the previous design presents the values of κ ranging from -7.2 to 3.3 pm/mN, the κ values of the new design spans from 0.61 to 3.0 pm/mN. This demonstrates the potential of the new flexure to provide improved independent axial force sensing. Second, Fig. 9(c) shows a smooth variation of κ as the force direction changes, without the humps as shown in Fig. 9(a). This could explain why the second-order Bernstein polynomial can provide a good estimate for the previous design, yet is unable to model the fluctuations of the new tool.

B. Current Issues and Future Improvements

While the FEA simulation predict improvement on decoupled axial force sensing with this new design, the experimental results are difficult to model with a linear regression or second-order polynomial. Compared with the previous design [19], the new sensor design should provide a refined flexible structure. However, it also presents challenges on fabrication. The assembly model is devised to build a prototype as a proof of concept. In the assembly design, additional assembly tolerances are included when dimensioning the components, in order to allow manual assembly of a dozen of components with micron-level dimensions. More than 20 adhesive bondings are used to join 12 components within a $\varnothing 0.9 \times 8$ mm volume. The force sensor prototype built is very different from the ideal FEA simulation model. However,

the new design of the 3-DOF force sensing instrument does show the potential to achieve better axial force sensing. As shown in Section IV-A, the variation of κ is suppressed into a fairly small interval. Improving the fabrication process would be important to enhance the sensing performance, e.g., reducing noises, and minimizing the peaks and valleys shown in Fig. 9(a). We are considering adopting MEMS techniques to fabricate the flexure as one single part, eliminating the error-prone manual assembly process of the flexure. Design parameters can be optimized for the MEMS process, in order to improve the axial force sensitivity, as well as to enhance the sensing decoupling and noise rejection. The parameters include width and thickness of the Y-shape flexure beams, as well as the distance between the two sets of the flexure beams.

V. CONCLUSIONS

Lack of force sensing is one of the most formidable technical challenges in retinal microsurgery. Previous work by our group has investigated 2-DOF and 3-DOF force sensing instruments with fiber optic sensors. This paper presents the development of a new 3-DOF force sensing ophthalmic tool with FBG sensors. The force sensing is integrated into the distal portion of the tool shaft with a diameter of 0.9 mm and a length of 8 mm. A new flexure is designed to achieve high axial force sensitivity and low crosstalk noise from transverse force. An assembly model is devised to prototype the force sensor. The assembly components are fabricated using photochemical etching and laser micro-machining, and manually assembled under microscope. Extensive calibration with force loads up to 21 mN in 168 force directions is carried out using an automated calibration system. Experiment results show that the new 3-DOF force sensing instrument can provide transverse force measurement with 0.5 mN RMS error using a linear model, and axial force measurement with 3.3 mN RMS error using a second-order Bernstein polynomial model. A few observations of the behavior of the inner FBG sensor could provide explanations for the sensing performance of this new tool. They could also suggest possible measures to improve future iterations. As a proof of concept, this new design has demonstrated the potential to enhance independent axial force sensing. To further improve the sensing performance, advanced MEMS techniques will be used to increase the fabrication precision and accuracy. Future work includes more benchtop validation experiments, as well as *in vivo* experiments. The design of the 3-DOF force sensing tool can also be adopted for other surgical applications, where high resolution force sensing is desired at the tool tip with miniature size constraint. It can be used for distal force sensing in microsurgeries such as vascular and cochlear implant surgeries, as well as in catheterization procedures.

REFERENCES

- [1] P. Gupta, P. Jensen, and E. de Juan, "Surgical forces and tactile perception during retinal microsurgery," in *International Conference on Medical Image Computing and Computer Assisted Intervention*, vol. 1679, 1999, pp. 1218–1225.

- [2] A. Menciassi, A. Eisinger, G. Scalari, C. Anticoli, M. Carrozza, and P. Dario, "Force feedback-based microinstrument for measuring tissue properties and pulse in microsurgery," in *IEEE International Conference on Robotics and Automation*, 2001, pp. 626–631.
- [3] J. Peirs, J. Clijnen, D. Reynaerts, H. Van Brussel, P. Herijgers, B. Corteville, and S. Boone, "A micro optical force sensor for force feedback during minimally invasive robotic surgery," *Sensors and Actuators A: Physical*, vol. 115, no. 2-3, pp. 447–455, 2004.
- [4] U. Seibold, B. Kubler, and G. Hirzinger, "Prototype of instrument for minimally invasive surgery with 6-axis force sensing capability," in *IEEE International Conference on Robotics and Automation*, 2005, pp. 496–501.
- [5] P. Polygerinos, L. D. Seneviratne, R. Razavi, T. Schaeffter, and K. Althoefer, "Triaxial catheter-tip Force sensor for MRI-guided cardiac procedures," *IEEE/ASME Transactions on Mechatronics*, vol. 18, no. 1, pp. 386–396, 2013.
- [6] P. Valdastri, K. Harada, A. Menciassi, L. Beccai, C. Stefanini, M. Fujie, and P. Dario, "Integration of a miniaturised triaxial force sensor in a minimally invasive surgical tool," *IEEE Transactions on Biomedical Engineering*, vol. 53, no. 11, pp. 2397–2400, 2006.
- [7] P. Baki, G. Székely, and G. Kósa, "Miniature tri-axial force sensor for feedback in minimally invasive surgery," in *IEEE International Conference on Biomedical Robotics and Biomechatronics*, 2012, pp. 805–810.
- [8] W.-T. Park, R. K. Kotlanka, L. Lou, M. Hamidullah, and C. Lee, "MEMS tri-axial force sensor with an integrated mechanical stopper for guidewire applications," *Microsystem Technologies*, vol. 19, no. 7, pp. 1005–1015, 2012.
- [9] P. Baki, G. Székely, and G. Kósa, "Design and characterization of a novel, robust, tri-axial force sensor," *Sensors and Actuators A: Physical*, vol. 192, pp. 101–110, 2013.
- [10] B. Bell, S. Stankowski, B. Moser, V. Oliva, C. Stieger, L.-P. Nolte, M. Caversaccio, and S. Weber, "Integrating optical fiber force sensors into microforceps for ORL microsurgery," in *International Conference of the IEEE Engineering in Medicine and Biology Society*, Jan. 2010, pp. 1848–1851.
- [11] P. Puangmal, L. D. Seneviratne, P. Dasgupta, and K. Althoefer, "Miniature 3-axis distal Force Sensor for Minimally invasive surgical palpation," *IEEE/ASME Transactions on Mechatronics*, vol. 17, no. 4, pp. 646–656, Aug. 2012.
- [12] P. Berkelman, L. Whitcomb, R. Taylor, and P. Jensen, "A miniature instrument tip force sensor for robot/human cooperative microsurgical manipulation with enhanced force feedback," in *International Conference on Medical Image Computing and Computer Assisted Intervention*, 2000, pp. 247–286.
- [13] A. S. Jagtap and C. N. Riviere, "Applied force during vitreoretinal microsurgery with handheld instruments," in *International Conference of the IEEE Engineering in Medicine and Biology Society*, vol. 4, no. 1, Jan. 2004, pp. 2771–2773.
- [14] I. Iordachita, Z. Sun, M. Balicki, J. U. Kang, S. J. Phee, J. Handa, P. Gehlbach, and R. Taylor, "A sub-millimetric, 0.25 mN resolution fully integrated fiber-optic force-sensing tool for retinal microsurgery," *International Journal of Computer Assisted Radiology and Surgery*, vol. 4, no. 4, pp. 383–390, June 2009.
- [15] X. He, M. Balicki, J. U. Kang, P. Gehlbach, J. Handa, R. Taylor, and I. Iordachita, "Force sensing micro-forceps with integrated fiber Bragg grating for vitreoretinal surgery," *SPIE Photonics West*, vol. 8218, no. 82180W, pp. 1–7, 2012.
- [16] I. Kuru, B. Gonenc, M. Balicki, J. Handa, P. Gehlbach, R. H. Taylor, and I. Iordachita, "Force sensing micro-forceps for robot assisted retinal surgery," *International Conference of the IEEE Engineering in Medicine and Biology Society*, pp. 1401–1404, Jan. 2012.
- [17] X. Liu, I. Iordachita, X. He, R. Taylor, and J. U. Kang, "Miniature fiber-optic force sensor based on low-coherence Fabry-Pérot interferometry for vitreoretinal microsurgery," *Biomedical Optics Express*, vol. 3, no. 5, pp. 1062–1076, May 2012.
- [18] B. Gonenc, J. Handa, P. Gehlbach, R. H. Taylor, and I. Iordachita, "Design of 3-DOF force sensing micro-forceps for robot assisted vitreoretinal surgery," in *International Conference of the IEEE Engineering in Medicine and Biology Society*, vol. 2013, Jan. 2013, pp. 5686–5689.
- [19] X. He, J. Handa, P. Gehlbach, R. Taylor, and I. Iordachita, "A sub-millimetric 3-DOF force sensing instrument with integrated fiber Bragg grating for retinal microsurgery," *IEEE Transactions on Biomedical Engineering*, vol. 61, no. 2, pp. 522–534, 2014.
- [20] X. He, D. Roppenecker, D. Gierlach, M. Balicki, K. Olds, P. Gehlbach, J. Handa, R. Taylor, and I. Iordachita, "Toward Clinically Applicable Steady-Hand Eye Robot for Vitreoretinal Surgery," in *ASME 2012 International Mechanical Engineering Congress and Exposition*, 2012, pp. 145–153.
- [21] A. Uneri, M. A. Balicki, J. Handa, P. Gehlbach, R. H. Taylor, and I. Iordachita, "New Steady-Hand Eye Robot with micro-force sensing for vitreoretinal surgery," in *IEEE International Conference on Biomedical Robotics and Biomechatronics*, 2010, pp. 814–819.
- [22] M. Balicki, A. Uneri, I. Iordachita, J. Handa, P. Gehlbach, and R. Taylor, "Micro-force sensing in robot assisted membrane peeling for vitreoretinal surgery," in *International Conference on Medical Image Computing and Computer Assisted Intervention*, vol. 13, Jan. 2010, pp. 303–310.
- [23] X. He, M. Balicki, P. Gehlbach, J. Handa, R. Taylor, and I. Iordachita, "A novel dual force sensing instrument with cooperative robotic assistant for vitreoretinal surgery," in *IEEE International Conference on Robotics and Automation*, 2013, pp. 213–218.